JTTEE5 5:419-430

Plasma Spray Forming: An Alternate Route for Manufacturing Free-Standing Components

A. Geibel, L. Froyen, L. Delaey, and K.U. Leuven

The present study uses plasma spray technology as a production process for the fabrication of free-standing, near-net-shaped NiAl components. Attention is especially focused on the in situ synthesis of NiAl. A new internal, dual powder injector blade has been designed to improve the gun performance as well as the spray efficiency of the feedstock powder. The specific role of the substrate (i.e., its shape and material) for the successful spray forming of free-standing parts is studied. The as-sprayed parts were subjected to a post-heat-treatment and hot isostatic pressing. Subsequently, they were metallographically inspected. The mechanical properties, such as hardness, Young's moduli, and the fracture behavior during four-point bending, are also examined.

Keywords hot isostatic pressing, mechanical properties, near-net-shaped components, NiAl synthesis, plasma spray technology

1. Introduction

THE DEMAND for more efficiency and cost savings has initiated an intensive search for materials that improve engine performance and lead to extensive weight savings at the same time. Great interest has been focused on a group of materials with promising properties, the intermetallics. Some aluminum-containing intermetallic compounds are not only low in density but also exhibit excellent phase stability up to the melting point. Moreover, they are very resistant against corrosion. These factors make them very suitable for use in aerospace applications, typically as components in turbine engines.

NiAl, which belongs to the group of intermetallics, has a density of 5.86 g/cm^3 and a melting point of 1911 K. It possesses an ordered body-centered cubic, B2 structure in a compositional range of 45 to 60 at.% Ni that is stable up to the melting point. Despite these promising properties NiAl suffers, like most other intermetallic compounds, from two drawbacks: the lack of ductility at low temperature and a poor creep resistance at high temperature (Ref 1). The lack of ductility at low temperature can be avoided by carefully controlling the microstructure (Ref 2). The poor creep resistance can be attributed to the enhanced diffusion in the B2 structure at elevated temperatures (Ref 2). Alloying NiAl with a second phase, such as FeAl or CoAl, improves the creep resistance (Ref 3).

The low ductility poses serious difficulties for the shaping of NiAl via conventional routes. Although the powder metallurgy route partially solves this problem for relatively small parts with a simple geometry, the problem is still unsolved for larger thin-walled parts. Plasma spray technology offers an alternate route. It combines the consolidation of the starting material to dense, near-net-shaped components with the benefits of high cooling rates in a single process step (Ref 4, 5).

A. Geibel, L. Froyen, L. Delaey, and **K.U. Leuven,** Department of Metallurgy and Materials Engineering, de Croylaan 2, B-3001 Heverlee, Belgium.

The present study focuses on the ability to use plasma spraying as a forming technology for the production of free-standing, near-net-shaped NiAl components. It was further examined whether the method can be used in combination with the material synthesis.

2. Experiment

Since aluminum-base intermetallics are prone to oxidation when plasma sprayed in air, all spraying was carried out in a low-pressure tank (Ref 6). The spray gun employed was an APS system from Metco, type 10MB with a maximum power of 80 kW.

Based on a suggestion of Boulos (Ref 7), an internal, dual injector blade, with two injector ports perpendicular to each other, has been designed to improve the efficiency of the plasma spray process. In Fig. 1 the injector blade design (Fig. 1a) is shown together with the resultant spray pattern (Fig. 1b). The injector blade was made of copper. A coupling ring ensured good thermal contact to the anode for cooling and retained the blade in place.

Two powders were used as starting material (see Table 1). The first powder, hereafter referred to as C1, was a commercial, water-atomized NiAl powder (Fig. 2a). The second powder was a blend of the powder C1 with a nickel-clad aluminum powder

Table 1 Properties of the powders used for plasma spray forming of free-standing, near-net-shaped NiAl components

Material	NiAl	Ni-clad Al	Blend: C1 & Ni-clad Al
Identification	C1	...	M1
Particle size range, μm	+40, –150	+53, –105	n.a.
Mean size, μm	85	105	n.a.
Composition, at.% Al			
Manufacturer	50	32.6	n.a.
XRD analysis	51.547	...	46.4
Density, g/cm^3			
XRD analysis	5.68	n.a.	n.a.
Experiment	5.62	n.a.	n.a.
Oxygen content, wt%	1.05	0.27	n.a.

n.a., not available

(Fig. 2b). The nickel-clad aluminum powder had a nominal composition of 67.4 at.% Ni, which corresponds with the two-phase area NiAl/Ni_3Al of the Ni-Al equilibrium phase diagram. The nominal composition of the powder blend was 53.6 at.% Ni and is well within the compositional range of NiAl. Powder C1 was used to investigate the spray deposition of free-standing components, whereas the powder blend was used to study the in situ synthesis of NiAl. The spray parameters employed are given in Table 2.

A simple rotary symmetric substrate was required for the production of plasma-sprayed free-standing components. However, the substrate had to meet several conditions: it had to be reusable, it had to withstand the high thermal impact from the plasma, and it had to be made of an easy-to-shape material. Furthermore, its coefficient of thermal expansion (CTE) had to be larger than the CTE of the deposit material.

A cylinder fabricated of stainless steel (type 316) served as the substrate (see Fig. 3a). A second substrate shape was used to demonstrate that it is also possible to produce more complex-shaped parts. The second design consisted of two blunt stainless steel cones that were attached to each other at the smaller ends of the cones (see Fig. 3b).

In order to monitor the substrate temperature during deposition, thermocouples (type K) were placed 2 mm below the surface near the ends of the cylindrical substrate. Prior to deposition, the substrates were lightly polished with an abrasive paper of a very fine grit size (paper 4000).

Specimens of the as-sprayed components were subjected to a furnace heat treatment at 1273 K under continuous argon gas flow for 21 h. A second set of specimens underwent a hot isostatic pressing (HIP) cycle at a pressure of 165 MPa for 2.5 h at a temperature of 1350 K. All specimens were prepared for metallography and subsequently inspected with light optical and scanning electron microscopy. The samples were etched with a solution of 25 mL HNO_3, 1 mL HF, and 49 mL H_2O.

The composition of the samples was determined from the lattice parameter a (Ref 8, 9), which was derived from x-ray diffraction (XRD) measurements by using Eq 1 and 2 (Ref 10). A second set of equations, 3 and 4, was applied to calculate the density ρ of NiAl (Ref 10): X_{ni} is the chemical composition of Ni expressed in at%).

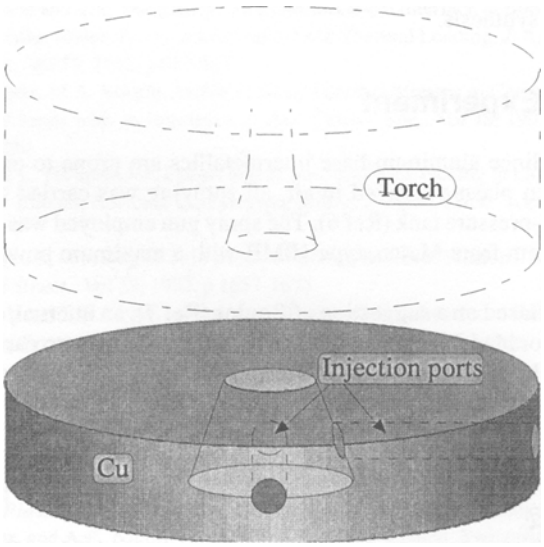

(a)

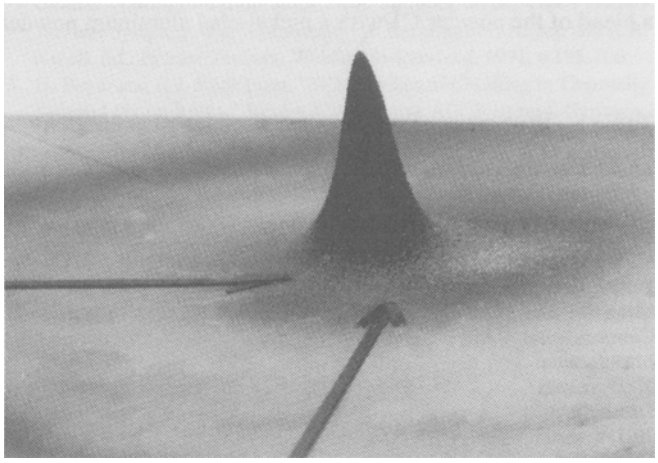

(b)

Fig. 1 Design of the modified dual injector blade, (a), which focuses the spray pattern, (b)

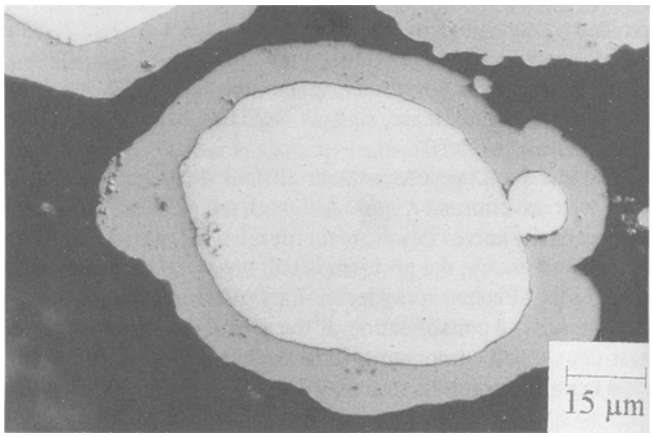

(a)

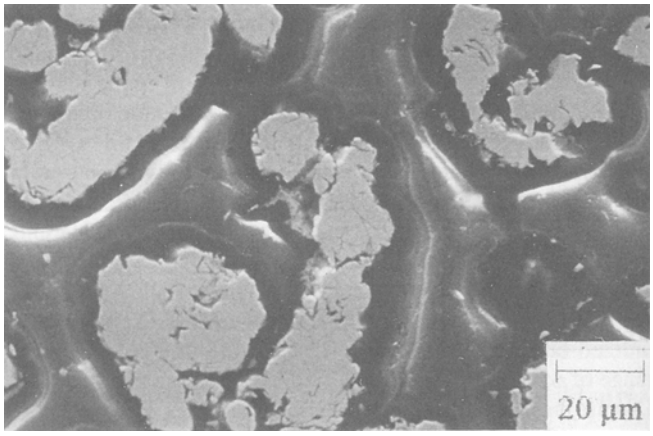

(b)

Fig. 2 Microstructure of the starting powders. (a) The prealloyed NiAl powder (HCST: Amperit 290.090). (b) The nickel-clad aluminum powder (Metco 404 NS)

$$a = 0.299839 - 2.22 \times 10^{-4} X_{Ni} \qquad 50 \text{ at.\%} \le X_{Ni} \le 60 \text{ at.\%} \qquad \text{(Eq 1)}$$

$$a = 0.266819 + 4.38 \times 10^{-4} X_{Ni} \qquad 45 \text{ at.\%} < X_{Ni} \le 50 \text{ at.\%} \qquad \text{(Eq 2)}$$

$$\rho = 3.15 + 5.5 \times 10^{-2} X_{Ni} \qquad 50 \text{ at.\%} \le X_{Ni} < 60 \text{ at.\%} \qquad \text{(Eq 3)}$$

$$\rho = 1.18 \times 10^{-1} X_{Ni} \qquad 45 \text{ at.\%} < X_{Ni} \le 50 \text{ at.\%} \qquad \text{(Eq 4)}$$

In addition to the XRD analysis, energy dispersive spectroscopy (EDS) was carried out on the metallographic samples.

For the as-sprayed samples as well as the heat-treated samples, gas analysis was carried out employing an automatic analyzer, EXHALOGRAPH EAO 202 from Balzers (Balzers, Hudson, New Hampshire). The specimens were preheated in a carbon crucible under vacuum at about 500 K to remove all adsorbed superficial contamination. A melting aid was added to the samples to ensure that all oxygen was thermally debonded. The released oxygen formed CO, which was subsequently analyzed. The device directly provided the oxygen content in parts per million with an accuracy of ±2%. From the oxygen content, the content of Al_2O_3 within the samples was calculated and further used to determine the density of the specimens.

The density of the samples was experimentally determined, according to the method of Archimedes, by submerging them into ethanol. The porosity (closed) was then determined by comparing the thus obtained density with the theoretical one.

Young's modulus was determined from four-point bending tests (Ref 11). The bending tests were carried out with a universal test machine, Instron 1196, with a maximum load of 250 kN. The constant cross-head speed was set to 8×10^{-4} mm/s[1]. The deflection of the specimen was recorded to an accuracy of 0.001 mm. The elastic moduli were derived according to the following equation (Ref 12):

Table 2 Summary of spray parameters for NiAl powders used for the production of free-standing components

Spray material	C1	M1
Substrate (stainless steel)	Cylinder & double cone	Cylinder
Carrier gas flow rate, L/min	5	5
Primary gas flow rate, L/min Ar(a)	41	41
Secondary gas flow rate, L/min H_2(a)	4	4
Power input, kW	32	32
Atmosphere at 10^4 Pa(a)	Ar/N_2	Ar/N_2
Spray distance, mm	117 ± 1	117 ± 1
Thermal condition of the substrate	Preheating	Preheating

(a) At operating temperature and pressure

$$E = \frac{Fa(3L^2 - 4a^2)}{4bh^3\delta} \qquad \text{(Eq 5)}$$

where E is the elastic modulus in bending (in pascals), F is the applied force (in newtons), L is the span length between the outer supports (in meters), a is the distance from the supports to the load applicator (m), b and h are the specimen width and height, respectively (in meters), and δ is the deflection at mid-span (in meters). The proof strength in bending, σ_p, is obtained from the equation:

$$\sigma_p = \frac{3F_p a}{bh^2} \qquad \text{(Eq 6)}$$

in which F_p is the load corresponding to the proof strength. The failed specimens of the four point bending tests were subjected to fractography. For each specimen group, C1 and M1, respectively, three bending experiments have been performed.

The microhardness of the samples was determined with a Vickers microhardness tester, applying a load of 300 g for 15 s. Ten measurements were taken for each specimen.

3. Results and Discussion

Examples of plasma-spray-formed, free-standing NiAl components are shown in Fig. 4. The parts were removed from the substrate without using a releasing agent or destroying the substrate. The wall thickness of the components varied from less than 1 mm to almost 10 mm. The inner surface showed perfect replication of the substrate surface.

3.1 *Temperature Evolution during Plasma Spraying*

The temperature evolution of the substrate during the deposition of the prealloyed NiAl powder, C1, and the powder blend, M1, is shown in Fig. 5. Each plot comprises the temperature curve recorded at the front end of the substrate. The plots are recorded for experiments that included preheating, deposition,

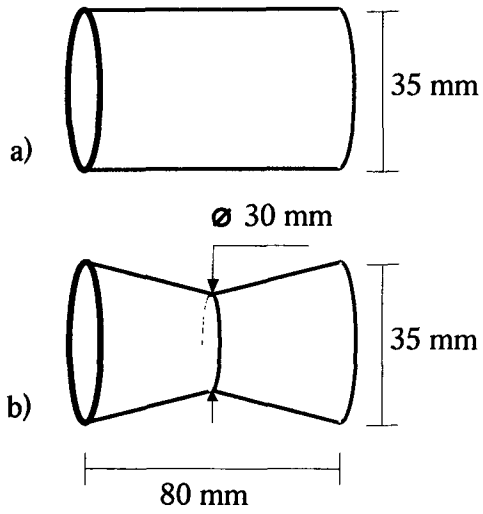

Fig. 3 Schematic drawing of the substrate shapes used for the production of free-standing NiAl components

and cooling sequences. Accordingly, three regions can be distinguished: the first and third region represent the preheating and the cooling of the substrate/deposit system, whereas the middle region represents the temperature evolution during deposition.

Preheating quickly raises the temperature of the substrate to a maximum, as indicated by the short plateau of the curve. The temperature has reached a stationary state in which the heat input from the plasma is balanced by conductive heat removal through the substrate and by heat loss due to radiation, which gains significance at higher temperatures. The cooling section shows the typical behavior for convective cooling in a gaseous environment.

The interesting part of the temperature curves is the temperature evolution during deposition. For both powders, the temperature rises at the beginning of the deposition. The largest source of heat input is the released heat of solidification from the impinging and solidifying splats. Initially, this large heat input cannot be removed fast enough because of the relative low thermal conductivity of the stainless steel substrate, which ranges from 16.2 to 21.5 W/m · K between 373 and 773 K. However, with increasing deposit thickness, the heat conduction through the deposit becomes more important. When the heat conduction of the substrate is matched by the conduction through the deposit, a steady state will be reached. For a larger heat conduction through the deposit, the temperature of the substrate will continue to rise. For the opposite situation, where the conduction through the deposit is lower than that through the substrate, the temperature of the substrate will slightly decrease.

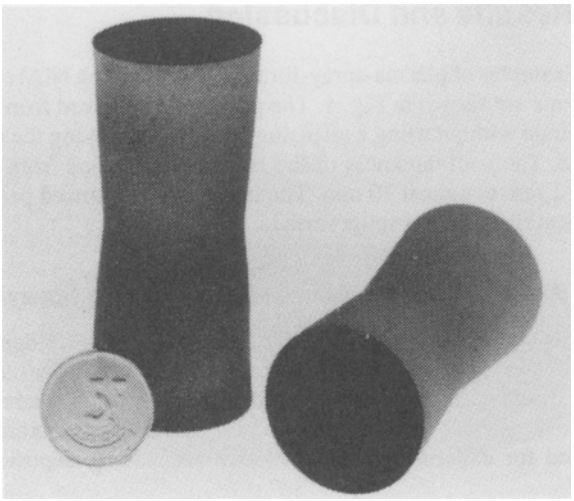

Fig. 4 Plasma-spray-formed NiAl, free-standing component

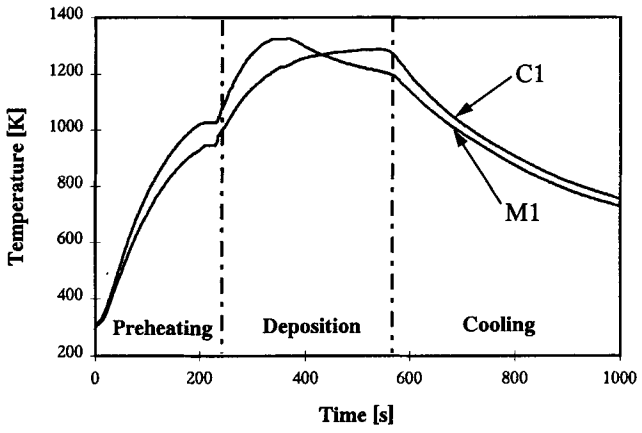

Fig. 5 The temperature evolution of the substrate during the deposition of the component C1 and the component M1

As can be seen in Fig. 5, there are differences between the temperature evolution during the deposition of the prealloyed NiAl powder, C1, and the powder blend, M1. During the deposition of the powder blend the temperature increase of the substrate is much steeper than that of the prealloyed powder. The steeper temperature rise of the former is attributed to the additional heat input from the exothermic reaction between the nickel and aluminum of the nickel-clad aluminum particles (Ref 13). Moreover, still unreacted nickel-clad aluminum particles will react on the hot substrate. The substrate temperature of ± 1273 K is more than sufficient to initiate the reaction that starts at 930 K (Ref 14).

While the temperature during the deposition of the prealloyed powder stays constant after this initial temperature increase, the temperature during the powder blend deposition starts to decrease. This temperature drop is related to the thermal conductivity through the deposit. With increasing deposit thickness, the heat conduction through the deposit becomes more important.

The heat conductivity depends on the heat transfer between adjacent lamellae and can be expressed by the thermal heat resistance, R (in units of K/W · m). R is a function of the material thermal conductivity, λ_s (in units of W/m · K), and the effective contact area of the lamellae, $2A$ (in square meters) (Ref 15). R is given as:

$$R = \frac{1}{2A\lambda_s} \qquad \text{(Eq 7)}$$

The effective contact area between two lamellae is the area where two adjacent lamellae are in intimate contact (see Fig. 6). The thermal properties of this region are considered to be equivalent to that of the bulk material. Due to interlaminar porosity the effective contact area is generally smaller than the total contact area of two adjacent lamellae. Therefore, the

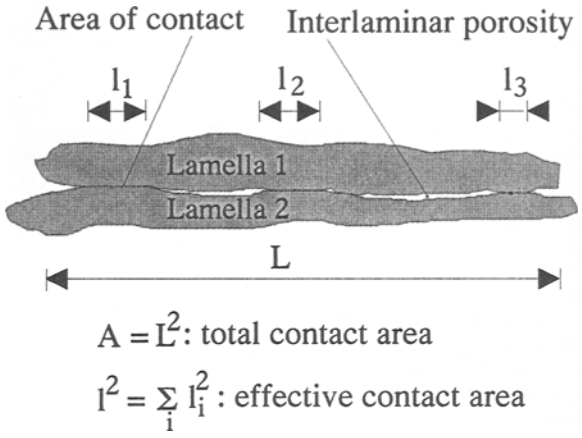

Fig. 6 Schematic representation of the effective contact area between adjacent lamellae within a plasma-spray-formed deposit

effective contact area is only a fraction of the total contact area. The interlaminar porosity is indeed observed in the as-sprayed components (see Fig. 7). Equation 7 is only valid when it is assumed that the contribution of heat transfer by conduction or convection across interlaminar gaps (porosity) is minor. Furthermore, the temperature within the deposit is assumed to be low enough so that radiative heat transfer across these gaps is also negligible.

Besides the porosity at the interlaminar boundary, adjacent lamellae are often separated by an oxide scale. The thermal conductivity is then the combination of the conductivity of the bulk and the oxide phase. The thermal conductivity of an oxide is generally lower than that of the bulk material. Hence, according to Eq 7, the larger the amount of porosity (A is small) and/or the higher the interlaminar oxide content, the higher the thermal resistance and the lower the heat conduction through the deposit.

Since the oxide content of C1 is higher than that of M1, a decrease of the temperature during deposition of the former was expected; instead, the temperature of the latter dropped. This behavior is attributed to the presence of Ni_3Al in M1 (see below) with a thermal conductivity of 35 W/m · K (Ref 16), which is about half that of NiAl, 80 W/m · K (Ref 17). Therefore, the overall thermal conductivity of M1 is considerably reduced with increasing deposit thickness. Thus, the increased thermal resistance results in the temperature drop of the deposit.

3.2 *Microstructural Evaluation*

The microstructures of the as-sprayed components C1 and M1 are shown in Fig. 7. The C1 powder deposit exhibits an inhomogeneous laminated microstructure with pores. The lamellae are often outlined by a stringer-like phase. EDS measurements showed that this phase had a large concentration of aluminum. In combination with back-scattered electron imaging the phase was identified as Al_2O_3.

At most places good contact was established between the impacting splat and the underlying lamellae. Due to this good contact, the heat extraction from the impinged splat was rapid and gave rise to fine columnar grains, 5 to 10 μm in size. The columnar grains seem to have grown across the oxide stringers separating adjacent lamellae. In the neighborhood of pores, however, the heat is slowly removed, providing enough time for the grains to adopt an equiaxed shape and grow to a relatively large size. At some places poorly molten or already resolidified particles are observed. These unmelts can be recognized by their round shape, often outlined by an oxide scale. They normally consist only of a very limited number of large grains.

The lamellae appear to have different compositions, since they reflect light with different intensities. Slight deviations from the stoichiometry to either side result in a change of the reflection behavior; nickel-rich NiAl appears brighter than aluminum-rich NiAl (Ref 13, 18, 19). Different grain orientations cannot explain this effect, because grains have grown across adjacent lamellae, which also show different brightnesses.

Also, sample M1 clearly exhibits a laminated structure consisting of lamellae with varying composition (see Fig. 7). Four different phases are distinguishable according to the brightness. The gray phase corresponds to the NiAl phase, the brighter phase indicates nickel-rich NiAl phases, and the brightest phase corresponds to Ni_3Al, as found from the XRD analysis (see Fig. 10). The fourth phase is Al_2O_3.

The formation of Ni_3Al can be attributed to an in-flight reaction of the nickel-clad aluminum powder particles. The formation reaction of Ni_3Al is an exothermic, self-propagating reaction that starts at 930 K (Ref 14). As Sampath et al. (Ref 20) have shown, the reaction is quite advanced but not always complete when the particles impinge the substrate. Due to the high deposit temperature (±1273 K), a diffuse transition zone has evolved between NiAl and Ni_3Al as the result of the diffusion of the constituents along the steep concentration gradients.

The Al_2O_3 stringers exhibit an accumulation at the NiAl phase, whereas the nickel-rich NiAl phases seem virtually oxide free. This preferential accumulation of Al_2O_3 can be understood in terms of the individual treatment a particle undergoes during plasma spraying. When a NiAl particle is heated to high temperatures or begins to melt, the aluminum instantly begins to oxidize (Ref 21) due to the oxygen present in the immediate surrounding atmosphere. The aluminum oxidation continues until the particle impacts the substrate, where rapid solidification terminates further oxidation. Before the aluminum oxidation in the nickel-clad aluminum particles can start, the nickel coating around the aluminum core must first melt. Mixing of the liquid nickel with the liquid aluminum core must occur before the alu-

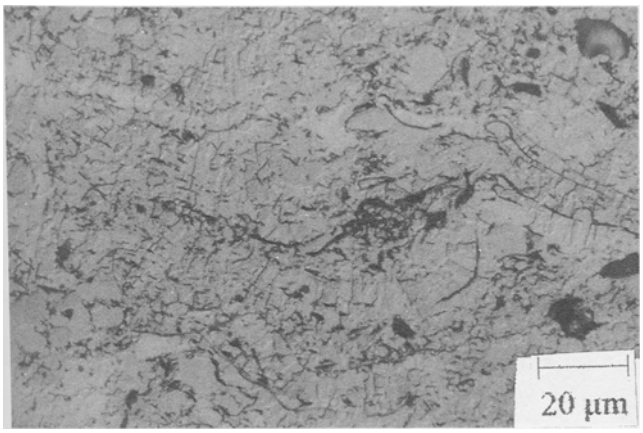

(a)

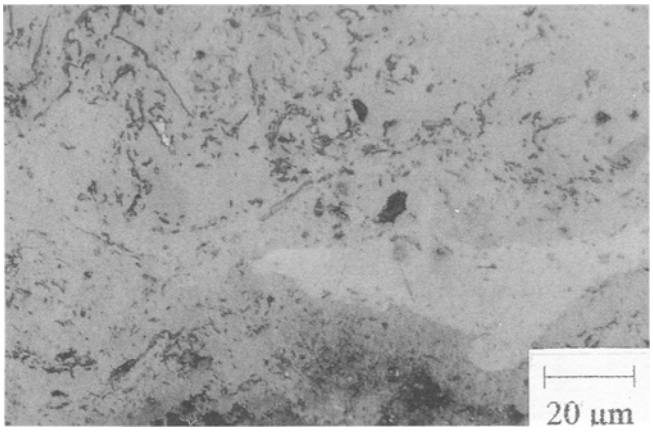

(b)

Fig. 7 Microstructure of the plasma-sprayed components. (a) C1. (b) M1

minum is exposed to the oxygen at the surface. Hence, it takes more time before the aluminum oxidation can commence. Consequently, a higher amount of Al_2O_3 is found with the NiAl phase formed from prealloyed NiAl particles as the feedstock.

In contrast to sample C1, M1 shows very few unmelted particles. This is attributed to the formation reaction of NiAl intermetallics. The exothermic heat of the reaction initiated during flight provides an additional heat source besides the plasma jet to thoroughly melt the particles in flight and ensures that they are liquid on impact. Moreover, particles that have not completed the reaction during the flight complete it on the substrate. When such particles are solid on impact they melt on the substrate and are incorporated into the underlying matrix. This released reaction energy locally increases the surface temperature (see Fig. 5), which promotes the spreading of newly arriving particles. Due to this local temperature increase, the deformability of the deposit may be locally enhanced, and newly arriving, solid particles may deform the underlying material and, hence, become closely incorporated into the matrix.

The microstructure of the annealed specimen C1 (21 h at 1273 K) is shown in Fig. 8(a). Annealing resulted mainly in a compositional homogenization; no nickel-rich areas were observed in the microstructure. Otherwise, little impact of the annealing on the microstructure was observed except slight transformation of the still dominant, fine, columnar grain structure into a more equiaxed one. An excessive grain growth during the heat treatment was impeded by the oxide stringers outlining the lamellae.

The microstructure of M1 after annealing (see Fig. 8b) revealed the complete disappearance of the Ni_3Al. Slight grain growth took place, resulting in grains with a more equiaxed shape and a size of about 10 μm. Although the oxide stringers also act here as growth barriers, they only slightly disturbed the diffusion of the constituents toward the compositional homogenization.

The microstructure after HIP, however, is drastically altered (see Fig. 9). As for the annealing, a complete compositional homogenization took place (the same gray level is observed throughout the microstructure). The grain structure has clearly changed. Considerable grain growth into a fully equiaxed structure occurred. The largest grain size is observed with sample M1 HIP. The size evolved from ~10 μm in the as-sprayed state to >25 μm. The least grain growth is observed with C1 HIP, where the initial grain size was ~10 μm and grew to ~15 μm.

Additionally, the oxide stringers have transformed into a uniform distribution of globular oxides. The oxide content is higher

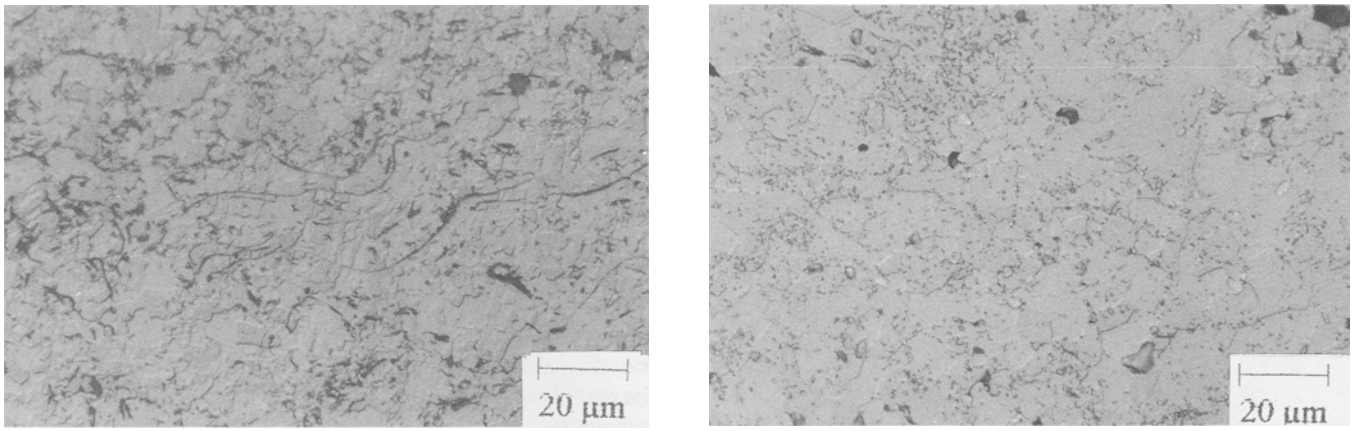

(a) (b)

Fig. 8 Microstructure of the plasma-sprayed components after annealing. (a) C1. (b) M1

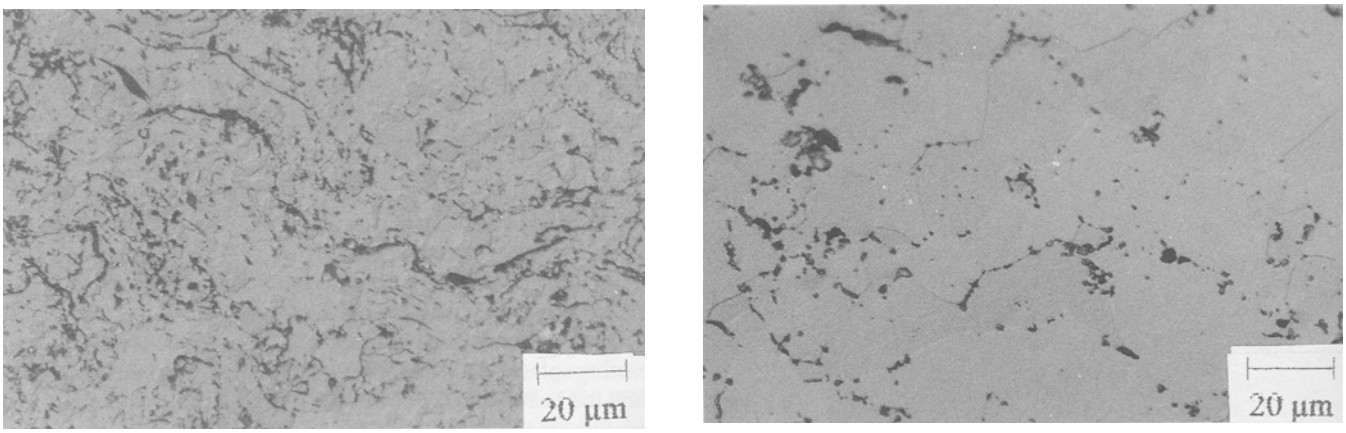

(a) (b)

Fig. 9 Microstructure of the plasma-sprayed components after HIP. (a) C1. (b) M1

in C1 HIP. The preferential location of the oxides in M1 HIP is along the grain boundaries.

It seems that the high amount of oxides is responsible for the restricted grain growth in C1 HIP. As long as the oxide stringers of C1 are not completely transformed during HIP into globular oxides, they act as growth barriers for grain growth. Due to the little amount of oxides in M1 and its nonuniform distribution, grain growth is only impeded at oxide accumulations. As a consequence, the porosity level observed for C1 HIP is higher than that of M1 HIP.

3.3 *Compositional Evaluation*

The XRD pattern of the as-sprayed component C1 as well as the annealed and HIP state are shown in Fig. 10, together with the pattern of the starting powder for comparison. The diffraction pattern of the NiAl phase is dominant. The peaks are slightly broadened due to the compositional inhomogeneity, as was also observed in the microstructure. Besides the NiAl pattern, a small peak in both the powder and the pattern of the as-sprayed deposit occurred. This peak was identified as the (200) Ni peak, corresponding to a Ni(Al) solid solution visible as a bright nickel-rich phase in the microstructures. The main (100) Ni peak is not detected due to overlapping with a high-intensity (110) NiAl peak.

After annealing and HIP, the XRD patterns showed little difference from the as-sprayed samples, except for the disappearance of the nickel peaks. The peak width of the NiAl was reduced, emphasizing the compositional homogenization. Two small new peaks occurred, however, after HIP. The peaks on either side of the (100) NiAl peak were identified as peaks belonging to α-Al_2O_3.

The XRD patterns of M1 (Fig. 11) show, besides the pattern of the NiAl phase, the pattern of the Ni_3Al phase. In general, the NiAl peaks are slightly broadened. A slight shift toward higher angles is also observed. The peak broadening can be attributed to the variations of the nickel concentration of the NiAl lamellae. The lattice spacing is reduced (Ref 22) due to the excess nickel, which consequently causes a shift to increased two-theta positions. After annealing and HIP, Ni_3Al has completely disappeared. The only phase detected is NiAl, except for two small Al_2O_3 peaks appearing in the spectrum of the HIP'ed sample.

In order to determine the composition of the samples, the lattice spacing was derived from the XRD two-theta peak positions. However, since the lattice parameter has its maximum at the stoichiometric composition and drops linearly to either side of this composition (Ref 23), it was necessary to establish by EDS analysis whether the compositions were nickel- or aluminum-enriched. The composition of the NiAl phase was calculated with Eq 1 or 2.

The EDS analysis has been carried out on metallographic specimens in an automated manner. Each spot of a predefined array of points on the sample surface was successively analyzed. From the obtained data the mean value was computed. However, with the present EDS analysis, light elements such as oxygen cannot be detected. The analyzed aluminum therefore had two sources, NiAl and Al_2O_3, and had to be corrected for the oxidized aluminum. The oxide amount was obtained by the oxygen analysis, assuming that all oxygen was bound to Al_2O_3. From the known amount of oxygen, the weight percentage of oxides and the amount of the oxidized aluminum was calculated. This result was used to correct the results from the EDS analysis.

From the EDS analysis the composition of all specimens was found to be nickel-rich. The compositions were determined by applying Eq 1 (Table 3). Also included in Table 3 are the values for the annealed NiAl powder, used as a reference material.

The nickel concentrations of the as-sprayed components were slightly above the stoichiometric 50 at.%. M1 shows a high nickel concentration, which is associated with the initial high nickel concentration (53.6 at.%) of the feedstock powder. The value of 58.78 at.% determined by XRD for NiAl is slightly

Table 3 Lattice parameter, calculated nickel-concentration, and calculated density of the as-sprayed components, as well as the heat-treated (HT) and hot isostatically pressed (HIP) components, in comparison with the starting NiAl powders

Sample	Lattice parameter, nm	Ni concentration, at.%	Theoretical density, g/cm³
Powder C1 HT	0.28869	49.93	5.852
C1	0.28866	50.35	5.879
C1 HT	0.28862	50.53	5.889
C1 HIP	0.28848	51.15	5.922
M1	0.28679	58.78	6.336
M1 HT	0.28675	58.98	6.346
M1 HIP	0.28654	59.90	6.397

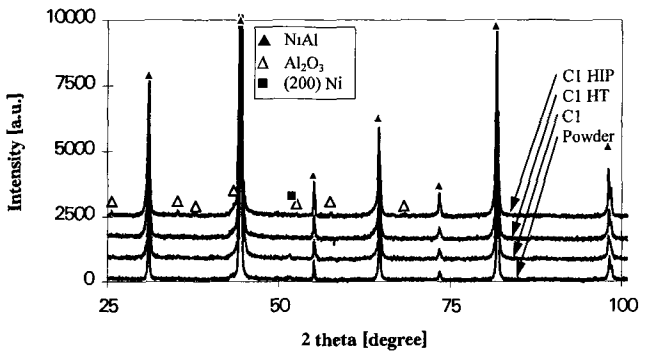

Fig. 10 XRD pattern of the plasma component C1 in its as-sprayed (C1), annealed (C1 HT), and HIP'ed (C1 HIP) state. For comparison the pattern of the starting powder is included.

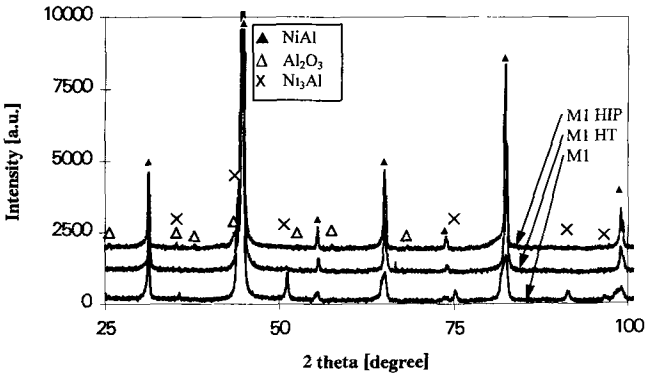

Fig. 11 XRD pattern of the component M1 in its as-sprayed (M1), annealed (M1 HT), and HIP'ed (M1 HIP) states

overestimated, because the sample is considered to comprise only NiAl, despite the presence of Ni_3Al. After annealing and especially after HIP, the nickel concentration is increased. During heat treatments, aluminum is lost due to oxidation, which results in a relative increase of the nickel content in NiAl. With the additional contribution from the dissolved Ni_3Al, a relative nickel content between 58.98 and 59.90 at.% after annealing and HIP is found, respectively.

The calculated porosity of the starting powders, and of the components in their as-sprayed, annealed, and HIP'ed state, is summarized in Fig. 12(a). In Fig. 12(b), the corresponding Al_2O_3 content is compiled.

Sample C1 exhibited 6% porosity, and no densification was observed after annealing or HIP. This can be related to the increased amount of oxides after annealing and HIP, which was 11% and 27% for C1. The oxygen penetrates the material by diffusion along grain boundaries and oxide/lamella interphase boundaries, where it reacts with aluminum to form Al_2O_3. The oxidation is accompanied by the inward injection of vacancies through the oxide scale (Ref 24). The accumulation of these vacancies at the oxide/NiAl interfaces leads in turn to the formation of new pores. On the other hand, the formation of Al_2O_3 results in a positive volume change that compensates for the gain of porosity.

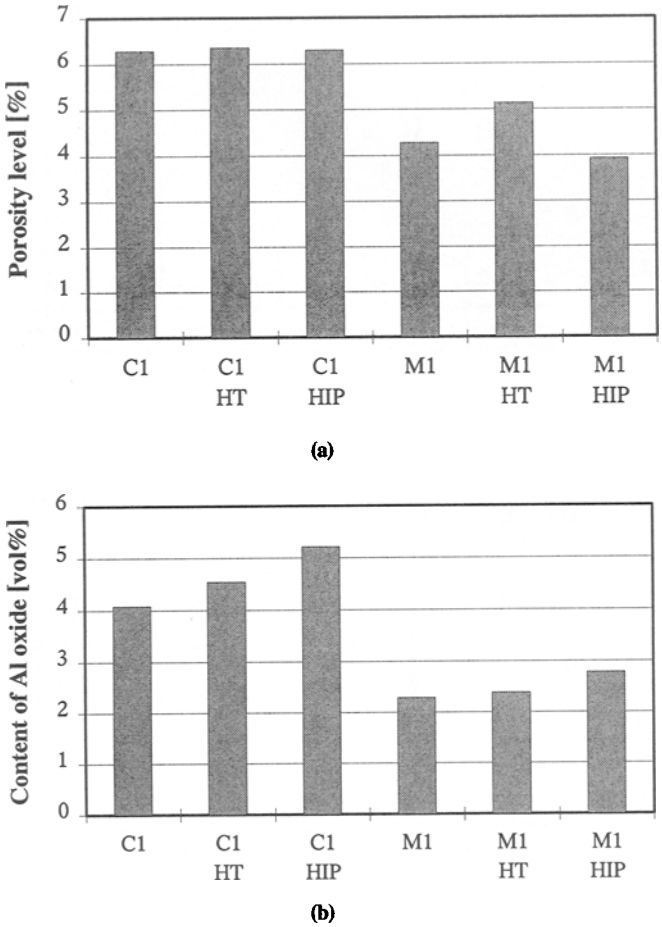

Fig. 12 (a) The porosity of the plasma-sprayed components in their as-sprayed, annealed, and HIP'ed states. (b) The Al_2O_3 content of the same

It is unlikely that oxygen is trapped within the pores of the as-sprayed components, because the plasma spray deposition was carried out in an inert gas atmosphere under reduced pressure. The most probably source of oxygen during annealing is the superficially adsorbed oxygen. HIP is carried out under an argon atmosphere with argon that has been recycled and that therefore may have accumulated considerable oxygen.

Due to the high-temperature/high-pressure condition, porosity is expected to be considerably reduced during HIP. The rate of porosity reduction depends, however, on the size of the initial pores. For a given temperature-pressure condition, the size of the pores that can be closed increases with increasing process time. If the initial pores are too large, they are only reduced in size. As observed in the microstructure, the initial pore size of sample C1 is relatively large. Evidently, the process time of HIP was too short to close all pores.

The theoretical density for M1 could not be derived due to the phase mixture of Ni_3Al and NiAl, of which the fractions are not accurately known. Instead, the theoretical density derived from the XRD measurement was applied and found to be >4%. For the annealed and HIP'ed specimens the theoretical value could be derived from the XRD measurements by applying Eq 3. After annealing the porosity was found to be slightly above 5%. It cannot be said with certainty whether this must be interpreted as an increase, especially when compared to the little-changed porosity of C1. In contrast to C1, the concentration gradients in M1 are large and may be considered equivalent to a driving force for enhanced diffusion. Hence, a diffusion-driven reduction of the porosity during HIP should be facilitated. Moreover, densification is facilitated by the presence of Ni_3Al, which has a lower creep resistance than NiAl. Hence, M1 showed a larger reduction in porosity to <4% after HIP. This is quite remarkable considering the initial large pore size, which was similar to that of C1. The pores would not be expected to be impeded since this sample had a low Al_2O_3 content.

Another source for porosity is process inherent. When a feedstock powder with a given size distribution is spray deposited, the injected particles always form a diverging spray cone (Ref 25). Some are led through the cold boundary regions of the plasma jet. These particles exhibit a low degree of melting (Ref 26, 27). A moving substrate will first intercept the particles in this boundary region, collecting a large number of particles with a low degree of melting. This entails the formation of protrusions and depressions, which leads to the formation of porosity. As the substrate penetrates deeper into the spray cone, particles with a higher degree of melting are deposited on top of these particles, forming layers with less porosity. As a result, the deposit often exhibits a layered structure with alternating bands of high porosity and bands of densely deposited material. This effect is more pronounced for feedstock powder with a broader size distribution.

3.4 *Mechanical Properties*

The microhardness of the as-sprayed and heat-treated components is presented in Fig. 13. The hardness of the as-sprayed components, C1 and M1, was found to agree well with the hardness reported for polycrystalline NiAl, $HV_{300} = 330 \pm 20$ (Ref 28). The hardness of M1 seems to reflect only the hardness of the

NiAl phase, despite the presence of the Ni_3Al (see Fig. 7), with a low hardness of $HV_{300} = 225$ (Ref 29).

Annealing increased the microhardness almost equally for both samples to values between $HV_{300} = 363 \pm 36$ and $HV_{300} = 388 \pm 85$. This increase can be attributed to the relative increase of the nickel concentration. NiAl in its stoichiometric composition exhibits the lowest hardness values, while deviation from stoichiometry to either side will increase the hardness (Ref 230.

HIP had no effect on the hardness of the sample C1 when compared to the as-sprayed state, whereas the hardness of M1 increased, even more than after annealing. Although the relative nickel concentration increased in C1 after HIP, the associated gain in hardness seems to be compensated by a softening effect due to the increased grain size, according to the Hall-Petch relationship (Ref 30), and the transformation of the oxide stringers into a more globular shape. The nickel concentration of M1 HIP approaches the upper limit of the nickel concentration for NiAl, which has the highest hardness (Ref 23). As with C1 HIP, a similar softening effect is expected. However, the effect of the high nickel concentration on the hardness seems to dominate the softening effect, as illustrated by the higher hardness value compared to that of the annealed state.

The Young's modulus, E, derived from the four-point bending test shows a somewhat erratic behavior (Fig. 14). While the value for C1 in the as-sprayed condition is 118 GPa, the value found for M1 is 178 GPa. An effect of the Ni_3Al in M1 on the mechanical behavior cannot be excluded. Since the Young's modulus agrees well with the modulus of Ni_3Al, 179 GPa (Ref 31), the mechanical behavior of M1 seems to be strongly influenced by the presence of Ni_3Al. After annealing, E decreased to about 100 GPa for both C1 and M1. After HIP the elastic moduli showed an increase to 120 GPa for C1 and 135 GPa for M1, respectively. This increase is attributed to the compositional and structural homogenization. For all conditions (as-sprayed, annealed, and HIP'ed), an influence of the Al_2O_3 on the elastic modulus is not readily observed.

The proof strength has also been determined by the four-point bending test, although it should be noted that the proof strength in bending is not necessarily equal to either the yield or fracture strength in tension (Ref 12). Due to the brittleness of NiAl, very little deformation was observed, and hence, the determined proof strength can be considered equivalent to the fracture strength of the material, which is given in Fig. 15. In addition, the fracture samples were analyzed by means of fractography. The fracture surfaces of the samples C1 and M1 are shown in Fig. 16. The fracture surfaces of the corresponding HIP'ed state are shown in Fig. 17.

Sample C1 (Fig. 16a) exhibits mainly a brittle, intergranular failure in combination with a delamination of adjacent lamellae that were separated by an oxide scale. Due to the high deposition temperature, which may be considered equivalent to an in situ heat treatment (Ref 32), the deposited material underwent a partial homogenization. This homogenization improved the interlaminar cohesion of adjacent lamellae that were not separated by an oxide scale. Transgranular fracture was observed to a small extent. Traces of large pores (~10 μm) are also observed on the fracture surface. The large pores and the interlaminar oxide scales form the weakest links when the sample is loaded in a bending test. Although the external load has not exceeded the fracture strength of the material, it is expected that stress concentrations produce failure at these weak links. Cracks in the brittle NiAl, once nucleated, will propagate with a small increase of the external load. The weak link failure gives rise to a low strength.

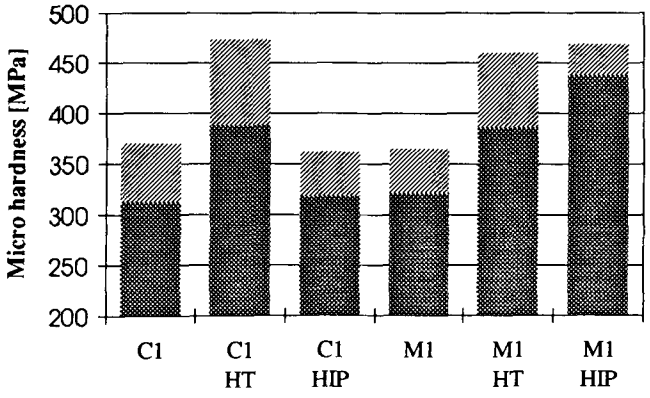

Fig. 13 The Vickers microhardness of the plasma-sprayed components in their as-sprayed, annealed, and HIP'ed states. The solid areas refer to the mean hardness values and the shaded areas denote the standard deviation.

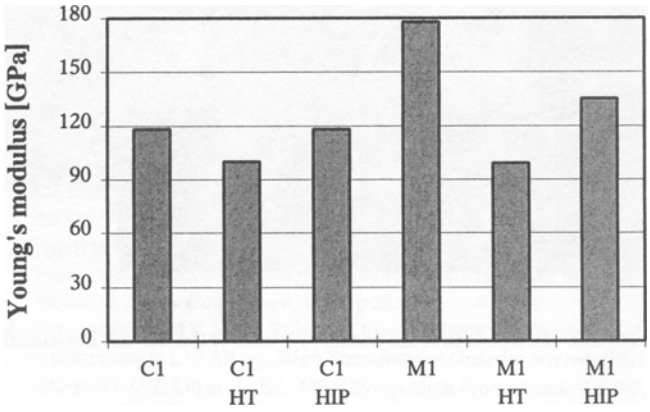

Fig. 14 Young's modulus derived from the four-point bending (solid bars)

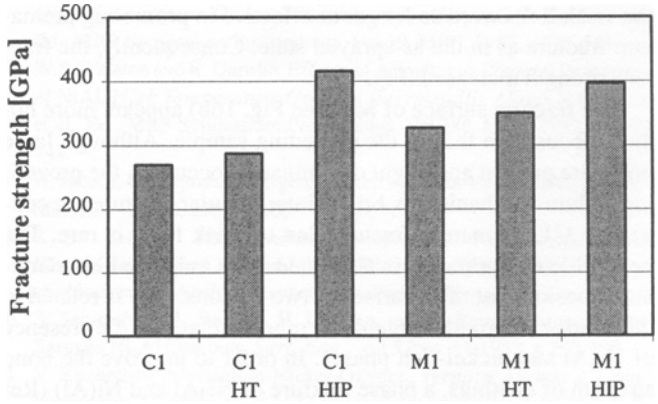

Fig. 15 The fracture strength of the free-standing components in their as-sprayed, annealed, and HIP'ed states

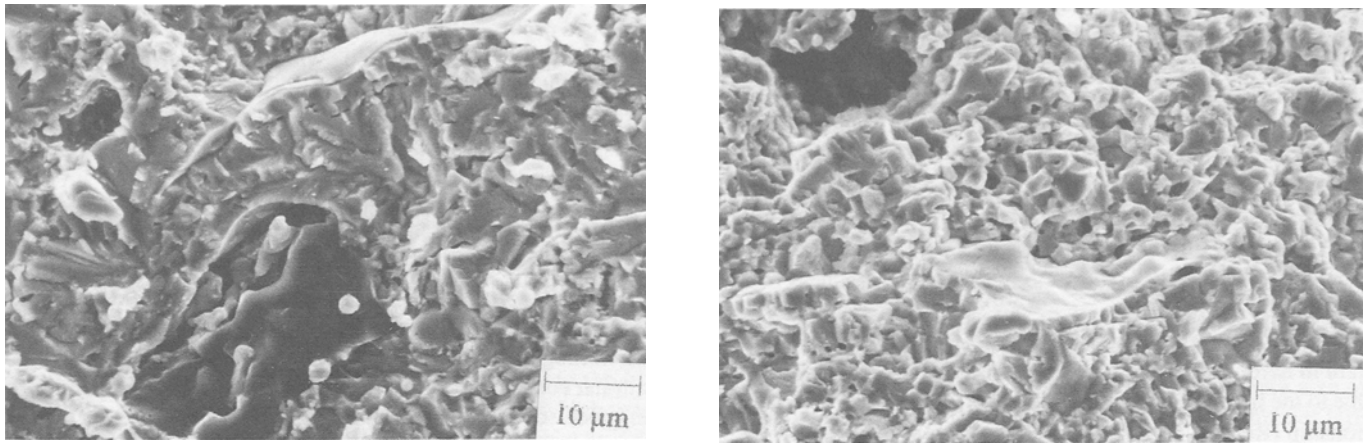

(a) (b)

Fig. 16 Comparison of the fracture surfaces of the as-sprayed components. (a) C1. (b) M1

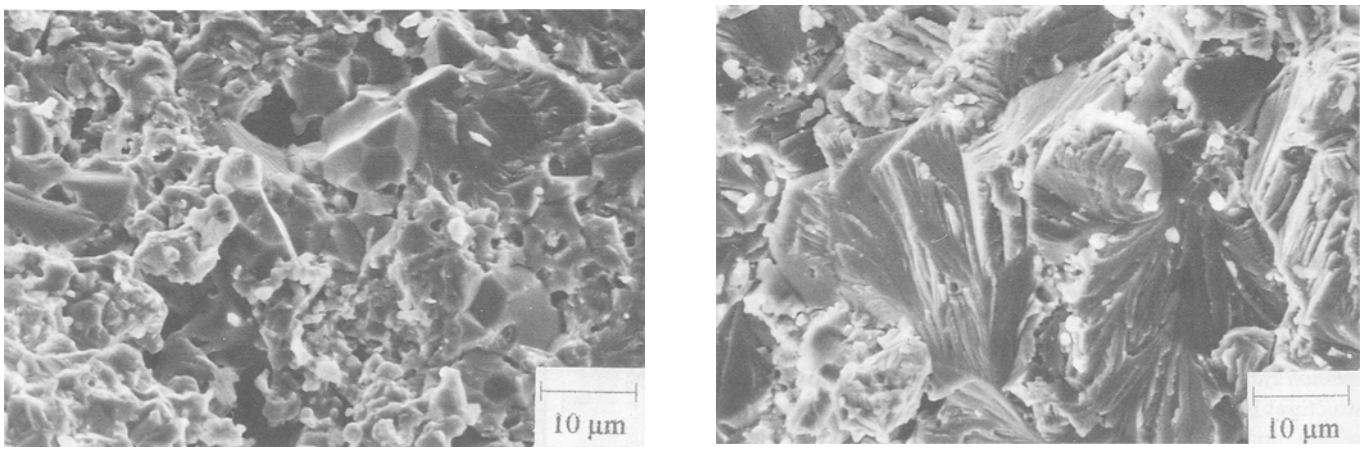

(a) (b)

Fig. 17 Comparison of the fracture surfaces of the HIP'ed, free-standing components. (a) C1. (b) M1

The compositional homogenization of C1 after annealing improved the interlaminar cohesion, which resulted in pronounced transgranular cleavage. Although traces of residual porosity, delamination, and intergranular fracture were still visible, the weak links were no longer as effective in promoting premature fracture as in the as-sprayed state. Consequently, the fracture strength increased (Fig. 15).

The fracture surface of M1 (see Fig. 16b) appears more homogeneous than that of the preceding sample. Although large pores are present and slight delamination occurred, the prevailing failure mechanism is brittle intergranular fracture. In contrast to C1, premature fracture due to weak links is rare. The negligible delamination is attributed to an enhanced interlaminar cohesion that might arise for two reasons. One is related to the relative low oxide content; the other is related to the presence of Ni_3Al and nickel-rich phases. In order to improve the bond strength of coatings, a phase mixture of Ni_3Al and Ni(Al) (Ref 33) is often applied. In the present case, Ni_3Al and the nickel-rich areas act in a similar manner. As observed in the microstructure, there is only a diffuse interface between Ni_3Al and NiAl. It is this continuous concentration change from one phase to the other that improves the cohesion. As expected, due to an improved interlaminar cohesion, the strength is higher than that of sample C1.

As indicated by the transgranular fracture and the reduced amount of intergranular fracture of M1 after annealing, the interlaminar cohesion increased, as was observed for C1. However, the beneficial effect of Ni_3Al on the interlaminar cohesion in the as-sprayed condition is lost due to the compositional homogenization. The small increase in fracture strength shows that the beneficial effect of the compositional homogenization overcompensates the effect of Ni_3Al in acting as a kind of interlaminar bond coat.

HIP of C1 continues the trend toward an increased fracture strength (see Fig. 16 and compare Fig. 17a). HIP entails not only compositional homogenization but also structural homogenization. Due to the changed oxide morphology, the grain structure transformation, and the reduction of the porosity, structural in-

homogeneities are no longer operative as sources for premature failure. As expected, the fracture strength is further increased compared to the annealed condition. Although HIP of M1 homogenized the relative composition and structure, the increase in fracture strength is lower compared to that of the HIP'ed sample C1. This can be attributed to the larger grain size of M1 HIP. The size is about double that of C1, which results in a reduced fracture strength according to the Hall-Petch relationship (Ref 30).

4. Conclusions

The present study shows that plasma spray deposition is a suitable technique to produce free-standing, near-net-shaped components of the difficult-to-shape NiAl intermetallic compound. If a prealloyed powder is used as feedstock powder, the composition of each individual particle deposited is retained. Moreover, this technique can also be used for in situ synthesis of Ni-Al intermetallic compounds in combination with the deposition to free-standing components. This was demonstrated by the deposition of a powder blend containing prealloyed NiAl and a powder comprising the elemental constituents nickel and aluminum.

For fabrication of the free-standing components, no mechanical anchoring of the deposit to the substrate is required, which makes preparation of the substrate (e.g., grit blasting) unnecessary. It was demonstrated that the deposits could be easily removed from the substrate without the use of a release agent or destruction of the substrate. This makes the substrate reusable for further spray deposition, a vital requirement for a cost-effective production route. If a substrate material is chosen that has a larger CTE than that of the deposit, the substrate contraction is larger than that of the deposit. The cylindrical shape of the deposit constrains that cooling contraction, which results in the evolution of a compressive stress. Eventually, this leads to the separation of deposit and substrate. This effect is even more pronounced when the substrate is heated prior to deposition.

During the deposition of the powders, some aluminum was oxidized. The Al_2O_3 formed stringers that had a detrimental effect on the mechanical properties of the deposits. In addition, a relatively high porosity level was found in the deposits. However, both the oxide content and the porosity level were low in the powder blend deposit. This is attributed to the released heat of the formation of Ni-Al compounds, which maintained the particles at a highly deformable state on impact. The nickel coating around the aluminum core acts as protection against excessive oxidation of the aluminum.

In order to improve the compositional and structural inhomogeneity and the mechanical properties, annealing and HIP were applied. Annealing only resulted in compositional homogenization. Hereby, the oxide stringers acted as growth barriers, stabilizing a fine-grained structure. The effect of the HIP was more pronounced. It transformed the detrimental stringer morphology of the oxides into fine, uniformly distributed globular particles, which are expected to act beneficially as particle reinforcement at high temperature. Another beneficial effect of HIP was the strong reduction of the porosity, which led to an increased cohesion. The HIP'ed samples also exhibited improved fracture strength, hardness, and elastic behavior, expressed by the increased Young's modulus.

Acknowledgments

The authors thank Dr. L. Buekenhout from IMT-Europe, St. Niklaas, Belgium, who carried out the HIP experiments. This study was sponsored by IUAP 41 action of DWTC (Belgium).

References

1. R. Darolia, NiAl Alloys for High-Temperature Structural Applications, *J. Met.*, Vol 43 (No. 3), 1991, p 44-49
2. G. Sauthoff, Intermetallic Phases as High Temperature Materials, *Z. Metallkunde*, Bd. 77, H. 10, 1986, p 654-666
3. G. Sauthoff, Intermetallic Phases—Materials Development and Prospect, *Z. Metallkunde*, Bd. 80, H. 5, 1989, p 337-344
4. S. Dallaire, Plasma Spray Forming of Coatings and Parts, *CIM Bulletin*, Vol 80 (No. 900), 1987, p 37-42
5. H. Herman, Plasma-Sprayed Coatings, *Sci. Am.*, Vol 9, 1988, p 78-83
6. A. Geibel, P. Verstreken, L. Froyen, O. van der Biest, L. Delaey, M. Poorteman, P. Barbary, and F. Cambier, Plasma Processing of Ceramic and Metallic Materials, *Atb Metallurgie*, 1990, p 111-119
7. M.I. Boulos, *International Summer School on Plasma Chemistry*, P. Fauchais, Ed., Italy, Sept 1989
8. A. Guinier, *Théorie et Technique de la Radiocristallographie*, 2nd ed., Dunod, Paris, 1956, p 396
9. R.D. Cullity, Elements of X-ray Diffraction, Addison-Wesley, 1967, p 363-375
10. R.D. Noebe, R.R. Bowman, and M.V. Nathal, Physical and Mechanical Properties of the B2 Compound NiAl, *Int. Mat. Rev.*, Vol 38 (No. 4), 1993, p 193-232
11. E. Macherauch, *Praktikum in Werkstoffkunde*, Auflage, Vieweg & Sohn, Braunschweig/Wiesbaden, 1989, p 224-228
12. Metals—Mechanical Testing: Elevated and Low Temperature Tests, *Annual Handbook of ASTM Standards*, Vol 03.01, Section 3, E 855, ASTM, 1984, p 788-803
13. O. Knotek, E. Lugscheider, and K.-H. Cremer, Alumina and Aluminide Formation in Nickel-Aluminum Spraying Powders, Paper 60, *Proc. Ninth Int. Spray Conference*, 1980, p 281-286
14. G.J. Ackland and V. Vitek, Effect of Ordering Energy on Grain Boundary Structure in L12 Alloys, *High Temperature Ordered Intermetallic Alloys III*, C.T. Liu et al., Ed., MRS Symposium Proceedings, Vol 133, MRS, 1989, p 105-111
15. R. McPherson, A Model for the Thermal Conductivity of Plasma Sprayed Ceramic Coatings, *Thin Solid Films*, Vol 112, 1984, p 89-95
16. R.K. Williams, R.S. Graves, F.J. Weavers and D.L. McElroy, Physical Properties of Ni_3Al Containing 24 and 25 Atomic Percent Aluminium, *High Temperature Ordered Intermetallic Alloys*, C.C. Koch et al., Ed., MRS Symposium Proceedings, Vol 39, MRS, 1985, p 505-511
17. W.S. Walston and R. Darolia, Effects of Alloying on Physical Properties of NiAl, *High Temperature Ordered Intermetallic Alloys V*, I. Baker et al., Ed., MRS Symposium Proceedings, Vol 288, MRS, 1993, p 237-242
18. H. Jacobi, Die Optischen Eigenschaften der Beta-Phase NiAl, *Z. Metallkunde*, Vol 60, 1969, p 106
19. K.-H. Cremer, Zur Reaktionskinetik von Nickel-Aluminium-Flammspritzpulvern, doctoral thesis, Rheinisch-Westfälische Technische Hochschule Aachen, Aachen, Germany, 1979
20. S. Sampath, G.A. Bancke, H. Herman, and R. Rangaswamy, Plasma Sprayed Ni-Al Coatings, *Surf. Eng.*, Vol 5 (No. 4), 1989, p 293-298
21. V. Kuznetsov, Aluminium-Nickel-Oxygen, *Ternary Alloys: A Comprehensive Compendium of Evaluated Constitutional Data*, Vol 7, G. Petzow and G. Effenberg, Ed., VCH Verlagsgesellschaft, Weinheim, BRD, 1993, p 434

22. A. Taylor and N.J. Doyle, Further Studies on the Nickel-Aluminum System, Part I: The β-NiAl and δ-Ni_2Al_3 Phase Field, *J. Appl. Cryst.*, No. 5, 1972, p 201-209

23. I. Baker and P.R. Munroe, Properties of B2 Compounds, *High Temperature Aluminides and Intermetallics*, S.H. Whang et al., Ed., The Mineral, Metal & Materials Society, 1990, p 425-452

24. R. Hutchings, M.H. Loretto, and R.E. Smallman, Oxidation of Intermetallic Compounds NiAl, *Metal Sci.*, Vol 1, 1981, p 7-13

25. M. Vardelle, A. Vardelle, and P. Fauchais, Spray Parameter and Particle Behavior Relationships during Plasma Spraying, *J. Therm. Spray Technol.*, Vol 2 (No. 1), 1993, p 79-92

26. R.W. Smith and D. Apelian, Melting Phenomena of Several Nickel Based Alloys in a Plasma Jet Operating at Low Pressure, MRS Symposium Proceedings, Vol 98, 1987, p 89-98

27. R.W. Smith, Particle Melting Behavior in a D.C. Plasma Jet: Observations on Several Nickel Based Alloys, *Thermal Spray Technology—New Ideas and Processes*, ASM International, 1988, p 123-128

28. R. Bohn, T. Haubold, R. Birringer, and H. Gleiter, Nanocrystalline Intermetallic Compounds—An Approach to Ductility? *Scripta Metall.*, Vol 25 (No. 4), 1991, p 811-816

29. X.R. Qian and Y.T. Chou, The Effect of Boron on Microhardness in Ni_3Al Polycrystals, *High Temperature Ordered Intermetallic Alloys III*, C.T. Liu et al., Ed. MRS Symposium Proceedings, Vol 133, MRS, 1989, p 529-536

30. E.M. Schulson and D.R. Barker, A Brittle to Ductile Transition in NiAl of a Critical Grain Size, *Scripta Metall.*, Vol 17, 1983, p 519-522

31. N.S. Stoloff, Ordered Alloys for High Temperature Applications, *High Temperature Ordered Intermetallic Alloys*, C.C. Koch et al., Ed., MRS Symposium Proceedings, Vol 39, MRS, 1985, p 3-27

32. K. Murakami, T. Okamoto, and Y, Miyamoto, Rapid Solidification and Self-Annealing of Fe-C-Si Alloys by Low Pressure Plasma Spraying, *Mat. Sci. Eng.*, Vol A117, 1989, p 207-214

33. R.H. Unger, Comparison of Thermal Spray Bond Coats, *Proc. Nat. Therm. Spray Conf.*, D.L. Houck, Ed., Orlando, FL, 1987, p 365-370